JCTC Journal of Chemical Theory and Computation

pubs.acs.org/JCTC Article

Ab Initio Insights into the Formation of Hydrated Dielectrons: Structure and Recombination Dynamics

José L. Guardado Sandoval, William R. Borrelli, Kenneth J. Mei, and Benjamin J. Schwartz*

Cite This: J. Chem. Theory Comput. 2026, 22, 4802−4812 Read Online

ACCESS | Metrics & More | Article Recommendations | Supporting Information

ABSTRACT: Despite extensive research on the behavior and properties of the hydrated electron (e^-_{hyd}), relatively little is known about the recombination of two hydrated electrons to form a hydrated dielectron. Hydrated dielectrons are hypothesized to be important in the radiation chemistry of water, particularly as an intermediate in the reaction that produces molecular hydrogen: $e^-_{hyd} + e^-_{hyd} + 2H_2O \rightarrow 2OH^- + H_2$. In this work, we investigate the solvation structures and recombination dynamics of both singlet and triplet hydrated electron pairs in bulk water using DFT-based *ab initio* molecular dynamics simulations. Our findings reveal that the recombination reaction leading to dielectron formation occurs exclusively from the singlet state, with the dielectron occupying a slightly larger cavity than the single electron. The potential of mean force for open-shell singlet electron pairs has a local minimum at a distance corresponding to a metastable state in which two electron cavities are separated by a single bridging water molecule. From this state, recombination to form dielectrons occurs by two distinct mechanisms: diffusive recombination and direct tunneling. These pathways have an approximately 1:1 branching ratio, a balance set by the symmetry of the local solvation environment. Diffusion occurs when both electrons experience similar, coupled solvation environments, while tunneling is triggered when asymmetric solvation destabilizes one electron, which then tunnels into the more stable cavity of the electron pair in a manner mediated by the bridging water molecule.

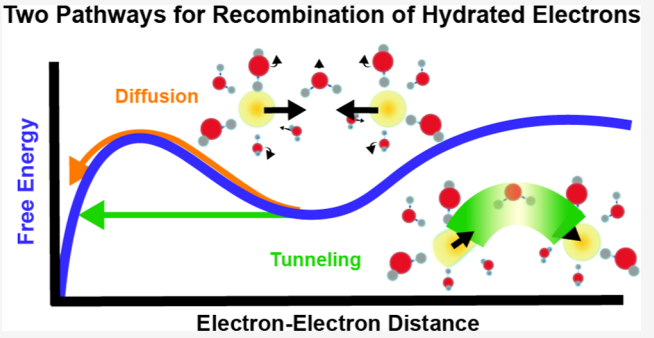

INTRODUCTION

Hydrated electrons (e^-_{hyd}'s), excess electrons that are solvated into cavities in liquid water, are among the most powerful aqueous reducing agents.[1,2] Hydrated electrons play crucial roles in areas such as radiation damage in biological processes,[3−6] nuclear reactors,[7−9] and water interfaces.[3,6,10−13] As a result, e^-_{hyd}'s have been a focal point of theoretical and experimental investigations for decades, including studies of their injection/relaxation dynamics,[1,6,10,14−18] solvation structure,[16,19−23] thermodynamic quantities,[24−31] absorption spectrum,[1,10,14] temperature dependence,[32,33] and reactivity with various substrates,[15,34] including reactions with potential leverage for environmental remediation.[35−37] Unfortunately, the same cannot be said for the hydrated dielectron ($e^{2-}_{2,hyd}$), which has been implicated in several solution-phase radiation chemistry processes,[14,38−42] but has never been directly observed,[43,44] despite predictions of its spectroscopic features.[30,43−46]

An important reaction in which $e^{2-}_{2,hyd}$ is implicated is the so-called dielectron hydrogen evolution reaction (DEHE), which results in the formation of molecular hydrogen by the following mechanism[47,48]

$$e^-_{hyd} + e^-_{hyd} \rightarrow e^{2-}_{2,hyd} \quad (1)$$

$$e^{2-}_{2,hyd} + H_2O \rightarrow H^- + OH^- \quad (2)$$

$$H^- + H_2O \rightarrow H_2 + OH^- \quad (3)$$

The first step in the DEHE reaction process, eq 1, is the recombination of two single hydrated electrons into a dielectron species.[42] Once $e^{2-}_{2,hyd}$ is formed, the subsequent proton transfers (eqs 2 and 3) involve interactions with neighboring water molecules.[48] It is experimentally known that the rate of the overall DEHE reaction is diffusion-limited with a reaction distance of 9 Å, exhibiting Arrhenius-like behavior up to 150 °C[49] and a preference for hydrogen over deuterium.[14,42] It is inferred that the two electrons in the dielectron must be in the singlet spin state, as triplet H_2 is unbound.[49] A key question, which we address in this work, is whether dielectrons exist as solvent-separated contact pairs of e^-_{hyd}'s or as single-cavity structures where both electrons occupy the same spatial orbital.

Received: February 5, 2026
Revised: April 22, 2026
Accepted: April 22, 2026
Published: April 30, 2026

Theoretical investigations, including recent work from our group,[48] have provided atomistic insight into the DEHE reaction mechanism[38,42,47,50,51] as well as predictions for future experimental work.[45] For example, Landman and co-workers simulated hydrated dielectrons in water clusters and found that for larger clusters, the electrons recombined rather than remaining on the surface.[50] In their single trajectory, the two proton transfers (eqs 2 and 3) occurred concertedly after the recombination to form $e^{2-}_{2,hyd}$ (eq 1). Bu and co-workers[47] performed *ab initio* molecular dynamics (AIMD) simulations with 64 water molecules under periodic boundary conditions and observed the recombination of singlet hydrated electron pairs to form $e^{2-}_{2,hyd}$ (eq 1) with an adiabatic energy release of approximately 0.5 eV. These workers reported reorganization energies of 0.64 eV for $e^{2-}_{2,hyd}$ and 2.04 eV for the electron pair; they also saw the two proton transfers occur sequentially rather than concurrently.

In previous work,[48] we simulated the injection of a second electron into the cavity of a pre-existing hydrated electron to explore the details of the two proton transfer reactions. We found that the first proton transfer (eq 2) is influenced by H-bond water chains that facilitate the rapid movement of newly formed OH^- away from the former dielectron, while the second proton transfer (eq 3) is controlled by the solvation of the newly formed hydroxide ion.[48] We also provided a detailed prediction of the spectroscopy of all of the reaction intermediates,[45] potentially allowing dielectrons, hydrated electron pairs, H^- and single hydrated electrons to be detected in multipulse pump/probe experiments.

For all of this work, however, the details of the mechanism underlying the recombination reaction, eq 1, including the energy barriers, role of water reorganization during recombination, and the recombination rate, remain unknown. Thus, the purpose of this paper is to address these questions using DFT-based *ab initio* molecular dynamics simulations. We investigate singlet and triplet hydrated electron pair solvation structures in bulk solution and explore the recombination and pairing process of hydrated electrons that lead to eq 1. We calculate potentials of mean force (PMFs) between hydrated electron pairs and find that spin singlet electrons form metastable contact pairs separated by a bridging water molecule, and that recombination into a single cavity takes place over a small free energy barrier of about 1 k_BT. In contrast, spin triplet hydrated electron pairs repel each other at all distances. Finally, we show that the recombination of singlet e^-_{hyd} pairs to form $e^{2-}_{2,hyd}$ proceeds both via diffusion-driven recombination and by tunneling-mediated recombination in which electron transfer is facilitated through the LUMO of the water bridging the two cavities. The presence of two recombination pathways may help explain the experimentally observed ∼9 Å reaction distance.[49,51]

METHODS

The DFT-based *ab initio* simulations of hydrated electron pairs and dielectrons presented here were performed using a system of 64 water molecules with periodic boundary conditions. We started using uncorrelated, equilibrated configurations of a 64-water system containing one excess electron from our previous DFT-based studies,[19,33,52] and then introduced a second excess electron with either the same (triplet) or opposite (singlet) spin. The simulations were performed with an identical methodology to our previous single excess electron work, allowing for direct comparison to the results presented here. Briefly, the simulations were carried out with the CP2K[53] software package in the *N*, *V*, *T* ensemble using a 0.5 fs time step and a Nosé-Hoover thermostat[54] to maintain a temperature of 298 K. Although the Nosé−Hoover thermostat was employed to maintain the canonical ensemble, we acknowledge that in the context of reactive trajectories, global thermostats can influence short-time dynamics or lead to slow equilibration of the reaction coordinate. However, the recombination events reported here depend on local structural and dynamical features that converge on shorter time scales. As such, although long-time ergodicity may not be achieved with our choice of thermostat, the results should be representative of the local thermal environment relevant to the hydrated electron recombination process that we study. Future studies might benefit from micro-canonical (*N*, *V*, *E*) ensembles or alternative stochastic thermostats to further isolate dynamical effects from thermostatting artifacts. The *N*, *V*, *T* ensemble was employed to ensure methodological consistency with established benchmarks for the hydrated electron pairs[45,47,48] and to maintain physical sampling of the recombination kinetics, as validated in previous studies.[31,55,56] The system volume was chosen to match the experimental density of liquid water at 298 K and 1 atm. DFT calculations were performed using the PBE0[57] functional with 25% exact exchange and Grimme's D3 dispersion correction.[58] We employed a triple-ζ basis set (TZVP) and a plane-wave cutoff of 500 Ry. Hartree−Fock exchange calculations were accelerated using the auxiliary density matrix method[59] with a cFIT3 basis.

We chose to use 25% exact exchange with the PBE0 functional because previous work has shown that this provides a reliable description of hydrated electrons,[19,33,45,52] and this choice also has been used to investigate the solvated electron-driven reduction of fluorocarbons.[60,61] Some prior studies showed that using 40% exact exchange, which better matches the experimental bandgap of liquid water, led to more reliable calculated adiabatic electron affinity values[47,62] relative to experiment.[63] However, there are minimal changes in the simulated structural and electronic properties with the two different choices of the amount of exact exchange used in the hybrid functional.[47,56,62] We acknowledge that the precise solvent structure and solvent reorganization energy may not be well represented by any DFT-based model, and that the results may vary slightly with different density functionals.[19,28,31,64−67]

To study the properties of colocalized hydrated dielectrons, we ran a total of 16 singlet state electron pair trajectories either until the DEHE reaction occurred or until a time of 2.1 ps if no reaction occurred. In this spin singlet case, we found that the second injected electron always immediately colocalized with the pre-existing hydrated electron into a single cavity. We also ran triplet state electron pair trajectories, which were equilibrated for ∼1−2 ps after the second electron localized into its own separate cavity. We note that previous hydrated electron studies have reported equilibration within 1 ps of electron injection, giving us confidence that our simulations were reasonably equilibrated.[68−70]

To prepare open-shell singlet (OSS) hydrated electron pairs for the study of eq 1, we took 22 uncorrelated equilibrated triplet electron pair configurations and flipped the spin state from triplet to singlet. Once the spin was flipped, these OSS electron pair trajectories were propagated for ∼3 ps (9 trajectories) or until recombination into a dielectron occurred (13 trajectories). In the 9 trajectories that did not recombine, we found that the two electrons were "stuck" along the diagonal of the simulation cell. Since this constitutes a finite size artifact, we did not include these trajectories in our ensemble averages. For trajectories with successful recombination, we observed that the structural changes were largely confined to the first solvation shell. Thus, although the finite size of our 64-water cell necessarily truncates long-range solvent polarization and modifies the dielectric screening of the electron−electron Coulombic repulsion, the fact that recombination is driven predominantly by nearby waters and proceeds through a local overlap of wave functions suggests that the primary driving force is correctly captured within this volume. Visualizations were done using VMD[71] with an in-house TCL script, and trajectory animations for representative trajectories are shown in the repository.

In previous work, we[19,33,52] and others[23,56] examined DFT-simulated hydrated electrons using either the spin density or the

https://doi.org/10.1021/acs.jctc.6c00228
J. Chem. Theory Comput. 2026, 22, 4802−4812

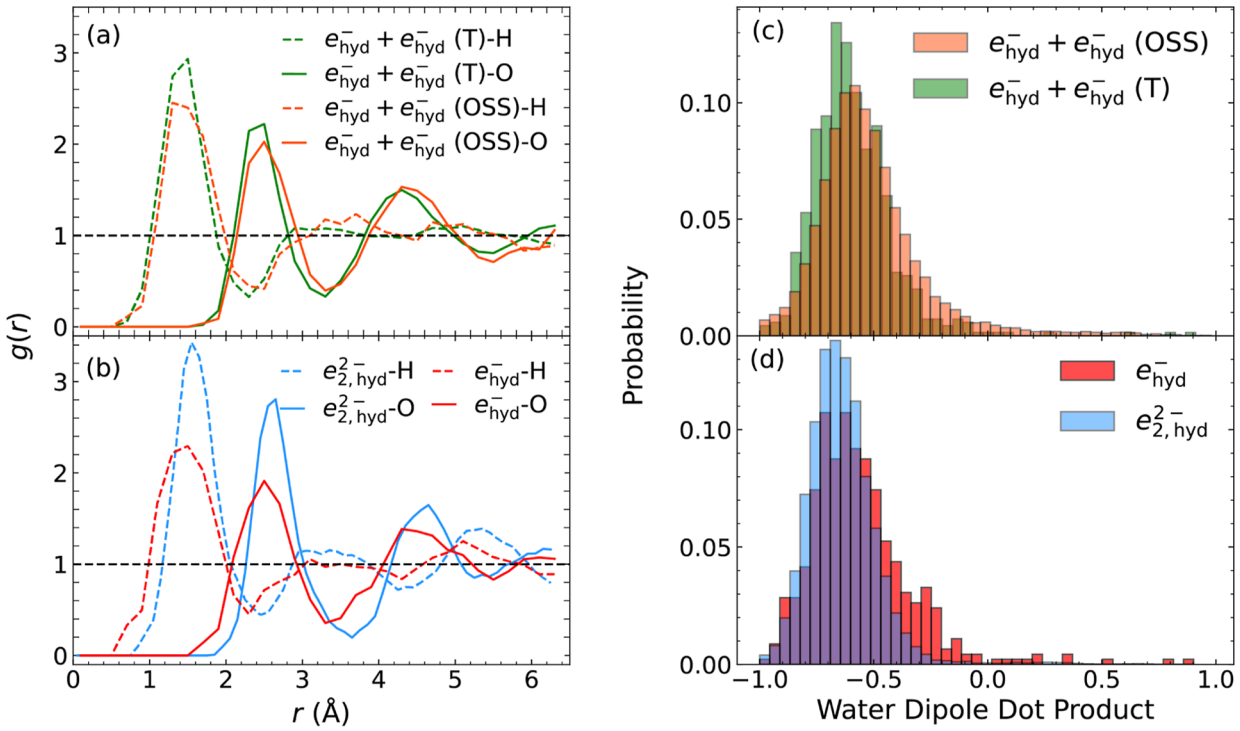

Figure 1. Radial distribution functions (RDFs or $g(r)$) and first-shell water angular distributions for hydrated electrons and dielectrons. Panel (a) displays e^--O (solid curves) and e^--H (dashed curves) RDFs for triplet ((T), green curves) and open-shell singlet ((OSS), orange curves) hydrated electron pairs. Panel (b) shows similar RDFs of $e^{2-}_{2,hyd}$ (blue curves) and the single e^-_{hyd} (red curves). Panels (c,d) show angular distributions of the first-shell waters for the four hydrated electron-based systems, where the water dipole dot product is that of a unit vector from the electron's center of mass to a first-shell water oxygen atom with a unit vector along that water's dipole. A result of −1 indicates solvation by the water dipole, while a dot product of ∼−0.7 is indicative of H-bond solvation. Panel (c) shows the first-shell angular distributions for (T) (green) and (OSS) (orange) hydrated electron pairs, while panel (d) shows the angular distributions for the single e^-_{hyd} (red) and $e^{2-}_{2,hyd}$ (blue). The RDFs and angular distributions of both electron pairs closely matches those of the single e^-_{hyd}, while those of $e^{2-}_{2,hyd}$ show a larger cavity with a more strongly defined local structure.

localized singly occupied molecular orbital (SOMO). Of course, there is no spin density for OSS hydrated electron pairs or for singlet dielectrons due to antiparallel spins, and the SOMO does not provide a meaningful spatial measure for either OSS or triplet e^-_{hyd} pairs due to the quasi-degeneracy of the two cavities. Therefore, we tracked the cavities of hydrated electron pairs using maximally-localized Wannier functions (MLWFs), with the electron positions taken as the Wannier orbital centers (WOCs) in the same fashion as in previous work.[45,47,48] These centers were used as the basis for (di)electron−water radial distribution functions (RDFs) and provided the electron−electron distances, $r_{1,2}$, needed to calculate PMFs. Recombination times for OSS trajectories were taken as the simulation time where the electron−electron distance reached zero. OSS electron pair density overlaps were computed as dot products of the normalized MLWFs.

To study the interaction of water molecules with each of the electrons in the OSS pair trajectories, we evaluated atomic configurations from our DFT simulations using the mixed quantum-classical TB pseudopotential model.[72,73] We calculated integrated TB potential values around each hydrated electron's WOC every 2.5 fs.[74] The calculation procedure involved generating a sphere of evenly spaced grid points within a 0.5 Å radius of each hydrated electron's WOC and then numerically integrating the TB potential evaluated on each grid point. We note that although the specific choice of grid size and cutoff radius changed the absolute values of the calculated potentials, the relative values were insensitive to these choices, so they did not affect the overall analysis or any of the conclusions, as described in the Supporting Information. For what is presented below, we used a grid with 20 points in each direction to balance the smoothness of the integrated potential with computational cost.

RESULTS AND DISCUSSION

We start our investigation of the molecular mechanisms underlying eq 1 by studying the solvation structure of different hydrated electron pairs. Figure 1 shows e^-−water oxygen (solid curves) and e^-−water hydrogen (dashed curves) radial distribution functions (RDFs or $g(r)$'s, panels a and b) and angular distributions (panels c and d) of spin singlet hydrated dielectrons (blue curves/bars), separate OSS (orange curves/bars) hydrated electron pairs, and spin triplet electron pairs (green curves/bars). For reference, Figure 1 also shows these same distributions for single e^-_{hyd}'s (red curves/bars) at the same level of theory.

Figure 1b compares the solvation structures of the e^-_{hyd} and $e^{2-}_{2,hyd}$. The structures are generally similar, but the dielectron occupies a slightly larger cavity than the single hydrated electron, consistent with its larger radius of gyration, R_g, of 2.91 ± 0.17 Å compared to 2.35 ± 0.09 Å for a single DFT-simulated hydrated electron.[48] These results are in good agreement with those reported in ref 47. Additionally, the larger R_g of the $e^{2-}_{2,hyd}$ is consistent with our recently published work predicting that the dielectron should have a detectable red-shift of its absorption spectrum relative to the e^-_{hyd}.[45] The sharper rise observed in the dielectron RDF indicates that the dielectron is confined within a "harder" cavity than the single hydrated electron. This DFT-simulated dielectron solvation structure is sharper than what was seen in previous dielectron studies using the mixed quantum-classical (MQC) approach.[75]

https://doi.org/10.1021/acs.jctc.6c00228
J. Chem. Theory Comput. 2026, 22, 4802−4812

Figure 1a presents RDFs for both triplet (e^-_{hyd} + e^-_{hyd}, (T)) and open-shell singlet state (e^-_{hyd} + e^-_{hyd}, (OSS)) hydrated electron pairs. The hydration structures and radii of gyration closely resemble those of single hydrated electrons, indicating that the electrons in these pairs behave essentially independently. In previous work,[45] we found that triplet and open-shell singlet electron pairs exhibit opposite trends in R_g as the distance between them decreases: for triplet hydrated electron pairs, R_g decreases because Pauli and Coulomb repulsion prevent overlap, while the R_g of OSS hydrated electron pairs increases because of favorable overlap of the electrons between cavities at close approach.

Figure 1c,d illustrates the angular distributions of first-shell water molecules around the single hydrated electron, dielectron, and different spin hydrated electron pairs. These distributions are calculated as the dot product of a unit vector from the electron's center of mass to a first-shell water oxygen atom and a unit vector along that water's dipole. With this definition, a dot product of approximately −0.7, as seen in all of the angular distributions, indicates H-bond coordination. The angular distributions of the electron pairs presented in Figure 1c strongly resemble that of a single e^-_{hyd} (panel d). In contrast, Figure 1d shows that $e^{2-}_{2,hyd}$ has a narrower distribution of first-shell solvent orientations than the single e^-_{hyd} or separated hydrated electron pairs, likely a consequence of increased solvent−solute interaction due to the placement of two charges in a single cavity.

With the structures of the species established, we turn next to studying the interaction between paired hydrated electrons with different spin configurations. Figure 2 presents PMFs for triplet (panel a) and OSS (panel b) hydrated electron pairs.

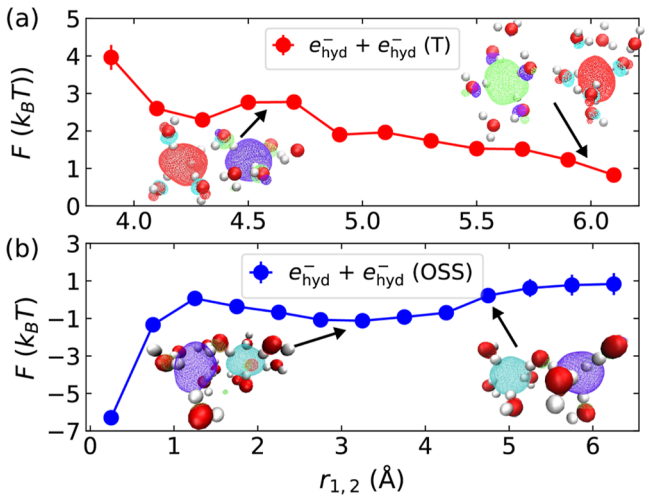

Figure 2. PMFs of hydrated electron pairs, plotted as free energy (F) (with standard error bars that are often smaller than the data points) versus distance between WOC's of the two electrons ($r_{1,2}$), for triplet (T) (red, panel a) and open-shell singlet (OSS) (blue, panel b) spin states. The PMF of (T) electron pairs in panel a shows purely repulsive behavior with decreasing $r_{1,2}$. The "bump" between 4.3 and 4.9 Å is the free energy cost to remove the bridging water molecule between the two cavities, as shown in the snapshot. In panel b, the PMF of (OSS) electron pairs shows a local minimum near a separation of ∼3.25 Å indicating stabilization by a bridging water molecule as seen in the corresponding snapshot. At even shorter $r_{1,2}$, there is only a ∼1 k_BT barrier to removing the bridging water, which induces subsequent recombination of the two hydrated electrons into a single cavity, forming a dielectron.

The PMFs were obtained by direct sampling of the distance between WOC's of the two electrons, $r_{1,2}$, with most initial separations starting in the range of 4−6 Å; here, the standard error was determined by bootstrapping via the SciPy library.[76] The zero of free energy for both profiles was established by shifting the long-range asymptote to match the expected screened Coulombic repulsion, $\kappa/r_{1,2}$, where κ represents the dielectric constant of DFT water with the PBE0 functional. The PMF of triplet-paired hydrated electrons (Figure 2a) shows overall repulsive behavior, a result that makes sense as spin parallel electrons experience both electrostatic and Pauli repulsion as the two cavities approach each other. The small additional barrier between 4.3 and 4.9 Å likely reflects the free energy cost to remove or reorient a single water molecule separating the two electrons.

In contrast, the PMF for OSS hydrated electron pairs (Figure 2b) is downhill at short $r_{1,2}$, indicating that recombination of these pairs into a solvated dielectron is energetically favorable. The local minimum near 3.25 Å indicates the existence of a metastable solvent-separated state,[49] the result of a single bridging water that simultaneously stabilizes both electron cavities by H-bonding, as shown in the inset snapshots of Figure 2 (as well as below in Figure 5). We see that there is a roughly ∼1 k_BT barrier, associated with disruption of the bridging water motif, for OSS electron pairs to surmount in order to recombine into a hydrated dielectron; this modest barrier is consistent with previous work.[47] Overall, however, it is energetically favorable for two spin-singlet paired electrons to combine, consistent with both our previous work[48] as well as others[47,50] studying the DEHE reaction, which found that OSS hydrated electron pairs quickly recombine into a single cavity.

The experimental measurements by Schmidt and Bartels[49] indicate that the recombination of hydrated electrons is a diffusion-limited process with an activation energy of ∼20.3 kJ/mol. This value corresponds to the diffusional barrier of the hydrated electron in bulk water, suggesting that the intrinsic chemical barrier for recombination upon encounter is negligible. Our computed barrier, to go from the metastable electron pair state to form the dielectron, which is approximately 1 k_BT or ∼2.5 kJ/mol is consistent with this "barrierless" encounter regime, particularly given that the two electrons in our simulations are effectively always inside the reaction distance even at their maximum separation. This is why the PMF in Figure 2b indicates that despite the natural Coulombic repulsion between electrons, there are no significant free energy barriers preventing recombination, highlighting the strong stabilization of the dielectron cavity relative to the single electron cavity. The absence of substantial free energy barriers throughout the simulated range is also consistent with the lack of ionic strength dependence on the reaction rate.[49,51] This suggests that once two hydrated electrons encounter each other within this range, the energetic landscape allows for a relatively uninterrupted approach toward the solvent-separated configuration and ultimately recombination.

Given that it is energetically favorable for OSS hydrated electron pairs to recombine, we next explored the precise mechanism underlying eq 1 and the corresponding rate of this part of the DEHE reaction. In the Supporting Information, we show the distribution of times to recombination based on the initial distances of the OSS electron pairs. However, since the OSS electron-pair PMF has a metastable state, we decided to

https://doi.org/10.1021/acs.jctc.6c00228
J. Chem. Theory Comput. 2026, 22, 4802−4812

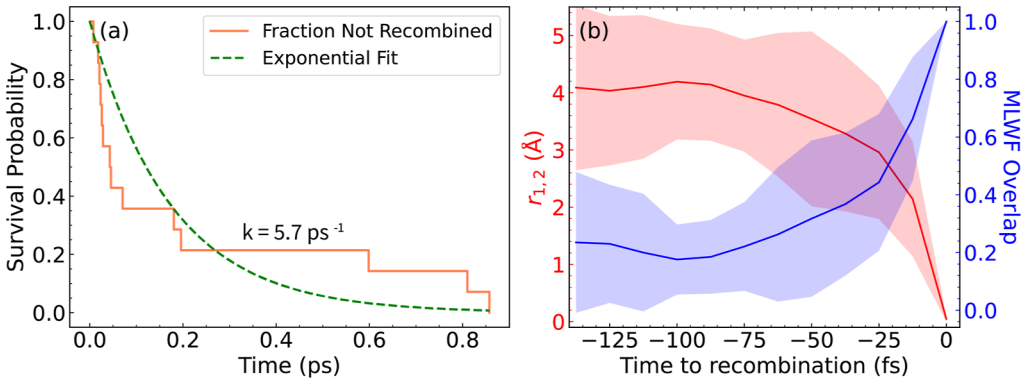

Figure 3. Kinetic analysis of the reaction of OSS hydrated electron pairs to recombine into hydrated dielectrons (eq 1). Panel (a) shows an electron-pair survival plot starting from the local minimum of the OSS spin state PMF ($r_{1,2} \approx 3.25$ Å). The *y*-axis represents the fraction of trajectories that have not yet recombined as a function of time. The dashed green curve is a single exponential fit with a rate constant of 5.7 ps^{-1}. Panel (b) shows nonequilibrium ensemble averages (curves) and standard deviations (shaded regions) of the electron−electron distance (red) and the maximally localized Wannier function (MLWF) overlap (blue) relative to the time of recombination defined as "0". Panel (b) shows that electron distance decreases and density overlap increases to form the dielectron only over the last ∼70 fs prior to recombination.

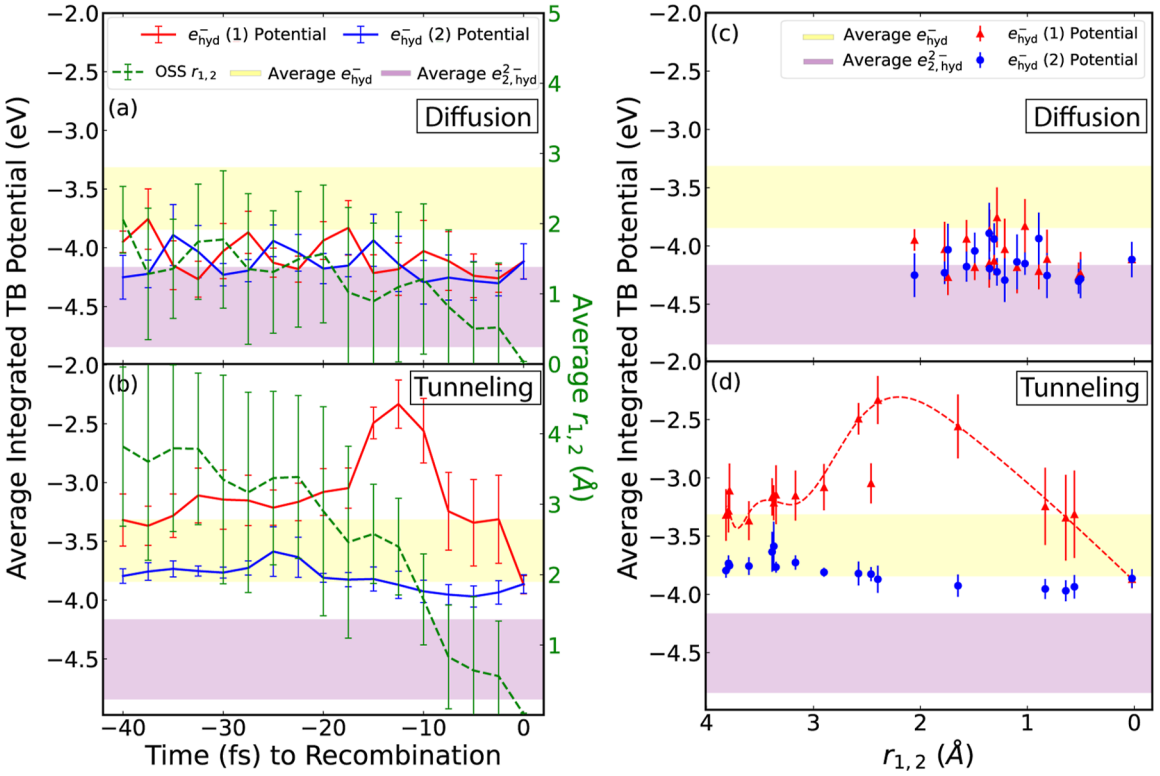

Figure 4. Subensemble-averaged TB potential (black *y*-axis) for the two e^-_{hyd}'s in an OSS pair and average $r_{1,2}$ distances between the hydrated electrons' Wannier centers (green *y*-axis) for the last ∼40 fs prior to recombination and dielectron formation (a,b). Average integrated TB potentials plotted against $r_{1,2}$ averaged over the 40 fs prior to recombination (c,d). Panel (a) shows the subensemble average for diffusion-driven recombination, while panel (b) shows that for tunneling-driven recombination. The purple and yellow shaded regions of each panel correspond to the calculated average TB potential values and standard deviations for the equilibrated $e^{2-}_{2,hyd}$ and e^-_{hyd} species, respectively. The red curves show the value of the integrated TB potential for the e^-_{hyd} experiencing the higher potential, while the blue curve shows the integrated TB potential for the lower-potential e^-_{hyd}. In diffusion-driven recombination, panels (a,c) show that both e^-_{hyd}'s experience similar solvation environments, even when they reside only ∼2 Å apart, when the two cavities are merging together. In contrast, in the tunneling pathway, the two electrons remain ≳4 Å apart until the last few tens of fs and experience significantly different local solvation interactions (panel b). In tunneling trajectories, the electron with the higher solvation potential is always observed to tunnel into the cavity of the electron with the lower potential. Panel d shows that the tunneling trajectories begin at $r_{1,2} \approx 4$ Å and have to cross a ∼2.5 Å wide and ∼1 eV high TB energy barrier to recombine. The red dashed curve is to guide the eye, and the barrier's presence supports the assignment of recombination in these trajectories as a quantum mechanical event.

focus on the kinetics of recombination starting from electron pairs separated at the distance of the PMF minimum. The results are shown as the orange survival probability trace in Figure 3a, where the *y*-axis represents the fraction of electron pairs that have not yet recombined as a function of time (i.e., a value of "1" means no trajectories have recombined and a value of "0" means that all trajectories have undergone recombination). The green dashed curve is a single exponential fit to the

https://doi.org/10.1021/acs.jctc.6c00228
J. Chem. Theory Comput. 2026, 22, 4802−4812

overall decay kinetics starting from the stable bridging water configuration at the PMF minimum; it has a decay rate of 5.7 ps^{-1}.

It is important to distinguish this value from the experimental diffusion-limited bimolecular rate constant of 6.0×10^9 M^{-1} s^{-1}.[49] By starting the trajectories near the PMF minimum (the bridging water configuration), we effectively bypass the long-range diffusion regime in order to provide an atomistic view of the short-range recombination mechanism. The high effective concentration (~1.7 M) inherent to our use of a 64-water cell allows us to sample these "inner-sphere" kinetics with high statistical frequency, revealing the role of bridging water fluctuations and wave function overlap that are otherwise averaged out in bulk kinetic measurements.

To better understand the computed rate constant, we turn next to examining the mechanistic details of the recombination event. Figure 3b displays the average time evolution of the MLWF overlap (blue curve with standard deviation shading) and the average electron−electron distance, $r_{1,2}$ (red curve with standard deviation shading), over the reactive OSS electron pair trajectories; the trajectories are aligned so that $t = 0$ is the recombination time, allowing us to track the dynamics at times immediately prior to recombination. The $r_{1,2}$ remains largely constant until approximately 70 fs before recombination, after which it rapidly decreases from ~4 Å, giving a more precise time scale for the actual molecular recombination event. Similarly, the average MLWF overlap remains minimal until the same ~70 fs before recombination, then increases as the electrons converge into the same cavity.

Although the average behavior in Figure 3 provides some information about the recombination kinetics, when we inspect the individual recombination trajectories, we see that there are actually two distinct recombination mechanisms. These two mechanisms are differentiated by the behavior of their MLWF overlap dynamics, which are shown explicitly for each trajectory in the Supporting Information. What we find is that some trajectories exhibit a gradual increase in MLWF overlap over more than a hundred fs prior to recombination, while others show an abrupt overlap increase in just the final few tens of fs, leading to the ~70 fs average behavior. To distinguish these two pathways, we noted that trajectories with $r_{1,2} \leq 3$ Å at a time 40 fs before recombination consistently displayed gradual MLWF overlap; we classify this subensemble as exhibiting "diffusive" recombination, reflecting the progressive translation and merger of water-separated cavities via coordinated solvation shell reorganization. In contrast, trajectories with $r_{1,2} > 3$ Å at a time 40 fs before recombination all exhibited a rapid MLWF overlap increase; we classify this subensemble as exhibiting "tunneling" recombination. Of the 13 trajectories that showed recombination, 6 proceeded via diffusion and 7 by tunneling, yielding an approximate 1:1 branching ratio. The green dashed curves in Figure 4 show the average $r_{1,2}$ behavior of each of these two subensembles, with panel a showing diffusive trajectories and panel b showing tunneling behavior; here, the error bars are the standard error for each subensemble.

We note that a few individual trajectories in both pathways exhibit kinetic recrossing events. In these instances, the electron pair temporarily sampled the dielectron configuration before returning to the metastable separated bridging-water state (see Figures S8 and S14 for representative trajectories that show this kind of feature). This behavior, which also has been observed in the reductive activation of CO_2 by hydrated electrons,[77] highlights the role of solvent fluctuations in modulating the final recombination step and further supports existence of a small barrier to recombination.

To further elucidate these two recombination mechanisms, in Figure 5 we visualized representative MLWF densities (blue and green wire mesh surfaces) of OSS hydrated electron pairs near the time of recombination, which as in Figure 4 we label

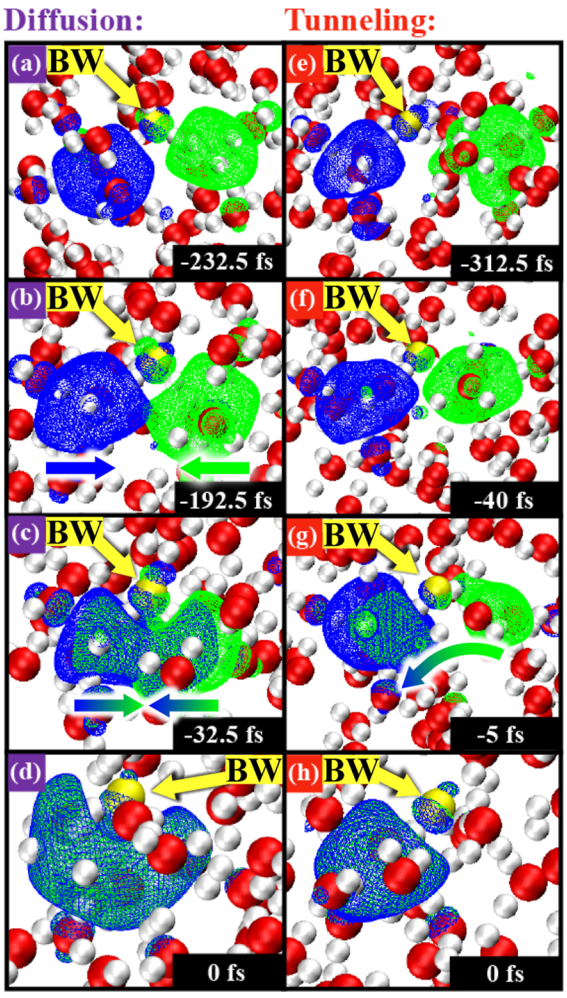

Figure 5. Snapshots of squared MLWFs for OSS hydrated electron pairs during two representative recombination trajectories, with $t = 0$ fs marking the recombination event, and the bridging water (BW) molecule depicted with a yellow oxygen atom. Panels (a−d) show diffusion-mediated recombination, while panels (e−h) illustrate recombination by tunneling. In the diffusion pathway, panel (a) shows the two electrons (blue and green mesh) occupying separate cavities, which begin to merge in panel (b) in the direction of the blue/green arrows. By panel (c), the densities of the two electrons almost completely overlap as the cavities continue to gradually combine. Finally, in panel (d), recombination is complete and both electrons occupy a single merged cavity. In the tunneling trajectory, panel (e) shows the two localized electrons in their separate cavities. This situation remains until 40 fs prior to recombination, panel (f), when the less solvent-stabilized electron (green mesh) begins to leak density into the cavity of the other electron (blue mesh) through the bridging water molecule. In panel (g), just 5 fs before recombination, a substantial portion of the less stable electron has tunneled into the more solvent-stabilized cavity in the direction of the blue/green gradient arrow, with complete recombination achieved by panel (h) where both electrons fully occupy the stable cavity.

https://doi.org/10.1021/acs.jctc.6c00228
J. Chem. Theory Comput. 2026, 22, 4802−4812

as time "0". Figure 5a–d shows snapshots from a representative trajectory in which recombination occurred through the diffusive mechanism. Panel (a) shows the two electrons residing in the local PMF minimum (cf. Figure 2 inset), where they are stabilized by a bridging water molecule whose oxygen atom is highlighted in yellow. Panel (b) shows an intermediate step in which the cavities of the two electrons have just begun to start merging with each other. In panel (c), the cavities have partially merged, and the two electrons are starting to occupy each other's cavities, increasing their overlap. In panel (d), we see the cavities have fully merged at the instant of recombination and the two electrons now occupy the same orbital, having become a (not-yet equilibrated) $e^{2-}_{2,\mathrm{hyd}}$. Thus, the diffusion-based pathway for eq 1 involves a combination of cavity translation and libration of the solvating waters. In the Supporting Information, we show similar animations of recombination events for all of the simulated trajectories.

Panels (e–h) of Figure 5 show snapshots of a recombination event via the tunneling mechanism. In panel (e), as in (a), the two electrons occupy the PMF minimum in adjacent cavities connected by a single bridging water molecule. At $t = -40$ fs, panel (f), the less stable electron (green) begins to leak density into its more stable partner's cavity (blue), which is still separated by the bridging water. In panel (g), 5 fs prior to recombination, the bulk of the less stable electron's density has funneled into the more stable cavity through the bridging water. Finally, at the instant of recombination, panel (h) shows that both electrons are colocalized in what had been the more stable single-electron cavity. This tunneling mechanism bypasses the translational reorganization of water molecules required to merge the cavities in the diffusion pathway, instead shuttling only one of the two e^-_{hyd}'s to create a hydrated dielectron. The rapid pair formation may be connected with the transient transport mechanism proposed by Lan et al. for single e^-_{hyd}'s,[78] who identified transient "ghost" cavities enabling jump-like transport. Our two-electron system suggests that water density fluctuations can facilitate wave function overlap not only into void cavities, but also into already-occupied ones.

To understand what determines whether eq 1 follows the tunneling or diffusive recombination pathway, we examined the local solvation environment experienced by each hydrated electron in the times preceding recombination. If one thinks of the recombination of two hydrated electrons as an electron transfer reaction, then Marcus theory would suggest that the solvent coordinate governing the reaction dynamics would be the electrostatic potential exerted by the surrounding water molecules on each electron. We found, however, that the average electrostatic potential from the surrounding waters on each electron was similar in the diffusion and tunneling pathways (as detailed in the Supporting Information), suggesting that a different local solvent coordinate must be involved.

Given that eq 1 involves the complete disappearance of one electron's cavity and the (slight) expansion of the other's cavity as the dielectron is formed, it would make sense that the local Pauli repulsive interactions between the electrons and their first-shell water molecules should also play an important role. Unfortunately, it is not straightforward to quantify the Pauli exclusion forces exerted on a hydrated electron from DFT simulations. Thus, to approximately account for both electrostatic and Pauli repulsion interactions between the electrons and the water, we used the Turi-Borgis (TB) pseudopotential.[72,73] The TB potential not only includes an electrostatic and polarization contribution but also accounts for the static exchange interactions between an excess electron and water molecules at the Hartree–Fock level of theory; this potential is commonly used in mixed quantum-classical simulations of hydrated electrons.[20,79−83] Thus, to estimate the total interaction between our simulated hydrated electrons and the surrounding waters, we took configurations from our DFT-based trajectories and then integrated the value of the TB pseudopotential (i.e., assuming that the DFT waters behaved classically) over a 0.5 Å radius sphere around each electron's WOC.

This integrated TB potential value serves as a local probe of the electronic stabilization energy, capturing the competition between the attractive electrostatic forces of the surrounding water and the repulsive Pauli interactions between the excess electrons and the electrons in the water molecular orbitals. A formal definition of the integration procedure we use and a detailed breakdown of the TB potential's individual components (electrostatic, polarization, and exchange) are provided in the Supporting Information. It should be noted that this potential analysis focuses exclusively on e^-_{hyd}–solvent interactions and does not include the direct e^-_{hyd}–e^-_{hyd} interactions. Thus, although the e^-_{hyd}-pair interactions are accounted for within the underlying DFT-based trajectories, our postprocessing TB integration is intended only to help quantify changes in the local solvation environment as the hydrated electrons approach each other.

The purple and yellow shaded regions in each panel of Figure 4 correspond to the calculated average integrated TB potential values, with a one standard deviation uncertainty, for the equilibrated $e^{2-}_{2,\mathrm{hyd}}$ and e^-_{hyd}, respectively, providing reference benchmarks for comparison with the nonequilibrium recombination trajectories. The blue and red curves in each panel (which correspond with the left y-axes) show the integrated TB potentials for each of the two electrons averaged over the diffusion (panel a) and tunneling (panel b) subensembles; graphs for each of the individual trajectories are shown in the Supporting Information. We plot the potential for the less solvent-stabilized electron in red and the more stabilized electron in blue. In the diffusion-driven recombination trajectories in panel (a), the potentials of both e^-_{hyd}'s remain similar within the uncertainty up through the point of recombination. In contrast, the tunneling recombination trajectories in panel (b) exhibit a clear divergence in the solvent-exerted potential on the two electrons. Thus, the way the water interacts with the electrons is clearly different in the two mechanisms of hydrated electron recombination.

The contrasting potential profiles reveal that the recombination mechanism is determined by the degree of solvation when electron pairs reach the PMF minimum. In diffusive recombination trajectories, the metastable bridging water configuration provides approximately symmetric stabilization for both electrons, so their integrated solvent potentials gradually converge from slightly below that of isolated single electrons (yellow shaded region) into the dielectron regime (purple shaded region) through coordinated librational and translational motions of the first-shell waters. Conversely, tunneling occurs when a strong solvation asymmetry develops from fluctuations in either the bridging water orientation, incomplete equilibration of the first solvation shells, or stochastic variations in water hydrogen-bonding networks. Any of these fluctuations serves to destabilize the solvent

https://doi.org/10.1021/acs.jctc.6c00228
J. Chem. Theory Comput. 2026, 22, 4802–4812

potential of one electron relative to the other. The characteristic solvent potential spike that occurs roughly 20 fs prior to recombination in tunneling trajectories seen in the red curve in Figure 4b results from the less-stable electron undergoing transient charge donation into the bridging water's LUMO as part of its rapid tunneling transfer into the more stable electron's cavity.

To further understand the nature of the recombination barrier, we plot the average integrated potential as a function of $r_{1,2}$, averaged over the final 40 fs leading to recombination in Figure 4c,d. For the diffusive trajectories, panel c, the potentials for both hydrated electrons remain relatively clustered and fluctuate within a narrow range at shorter separations, ($r_{1,2} \approx 2$ Å). In contrast, for the tunneling subensemble, panel d, there is a distinct energetic landscape where the two electrons occupy significantly different solvation environments even at larger separations ($r_{1,2} \approx 4$ Å). The destabilized electron (red) encounters a clear potential energy barrier as $r_{1,2}$ decreases. The dashed red curve is a trendline that highlights the effective tunneling potential barrier that has a ∼1.0 eV height and a ∼2.5 Å width. The presence of this barrier supports the tunneling assignment, and explains why these trajectories must recombine via tunneling rather than directly via diffusion.

As mentioned above, in the Supporting Information, we compare the results in Figure 4 with a similar calculation using only a purely electrostatic solvent potential, which shows no distinguishable difference between the diffusion and tunneling trajectories. This indicates that the main driving force that determines the mechanism of recombination arises primarily from Pauli repulsion and exchange interactions between the hydrated electrons and the electrons in the water molecular orbitals that are approximately accounted for with the TB potential. No matter how they recombine, the electron-pair system ultimately adopts the dielectron solvation structure (purple region), but the route to achieving recombination depends critically on Pauli repulsive forces in the local solvation symmetry of the metastable configuration.

CONCLUSIONS

In this paper, we presented a DFT-based simulation study of the recombination dynamics of two hydrated electrons to form a solvated dielectron (which then subsequently reacts with the surrounding water to produce H_2 and OH^-).[47,48,50] Analysis of radial distribution functions and radii of gyration confirm that both single hydrated electrons and hydrated electrons in pairs exhibit similar solvation structures, while the hydrated dielectron occupies a somewhat larger cavity with slightly more rigidly oriented first-shell waters. This structural similarity indicates that relatively little solvent reorganization is required for the recombination process, consistent with the sub-ps time scales for recombination observed in our simulations.

To characterize the free energy landscape governing recombination, we constructed PMFs for both triplet and OSS hydrated electron pairs. The triplet PMF is repulsive at all separations due to combined electrostatic and Pauli repulsion between parallel spins, with a modest barrier at 4.3−4.9 Å reflecting the free energy cost to disrupt solvent molecules intervening between the two cavities. In contrast, the OSS PMF is downhill at short distances, confirming that spin singlet electron pair recombination is thermodynamically favorable. A local minimum at $r_{1,2} \approx 3.25$ Å indicates a metastable solvent-separated configuration where a single bridging water molecule simultaneously stabilizes both electron cavities, separated by a ∼1 k_BT barrier from recombination into the dielectron state.

Time-resolved analysis of recombination dynamics from this metastable configuration revealed two distinct mechanisms that occur with approximately equal probability. The two recombination pathways are either diffusive, characterized by gradual increases in electron overlap over hundreds of femtoseconds, or via tunneling, exhibiting abrupt overlap development in just a few tens of femtoseconds. Our findings provide theoretical validation for the existence of a stable, solvent-separated singlet e^-_{hyd} pair hypothesized by Schmidt and Bartels from the lack of ionic strength effect in the DEHE reaction.[49] Moreover, the Pauli-repulsion-driven tunneling mechanism we observe, along with the sub-ps recombination time scale, are consistent with the experimentally observed reaction distance of ∼9 Å.[49,51] By enabling LUMO-mediated electron transfer across longer separations, tunneling effectively extends the capture radius beyond what diffusive cavity merger alone permits. This dual-pathway mechanism explains how the system achieves rapid recombination, overcoming Coulombic repulsion.

ASSOCIATED CONTENT

Data Availability Statement

Additional data for reproducing the results of this manuscript can be found in a persistent online repository (https://doi.org/10.5061/dryad.gmsbcc32c). This repository also includes representative input files to perform the calculations outlined in the Methods section.

Supporting Information

The Supporting Information is available free of charge at https://pubs.acs.org/doi/10.1021/acs.jctc.6c00228.

The Supporting Information contains a further description of the methods and simulation parameters used in this work (PDF)

AUTHOR INFORMATION

Corresponding Author

Benjamin J. Schwartz − *Department of Chemistry & Biochemistry, University of California, Los Angeles, California 90095-1569, United States;* orcid.org/0000-0003-3257-9152; Phone: (310) 206-4113; Email: schwartz@chem.ucla.edu

Authors

José L. Guardado Sandoval − *Department of Chemistry & Biochemistry, University of California, Los Angeles, California 90095-1569, United States*

William R. Borrelli − *Department of Chemistry & Biochemistry, University of California, Los Angeles, California 90095-1569, United States*

Kenneth J. Mei − *Department of Chemistry & Biochemistry, University of California, Los Angeles, California 90095-1569, United States*

Complete contact information is available at: https://pubs.acs.org/10.1021/acs.jctc.6c00228

Notes

The authors declare no competing financial interest.

https://doi.org/10.1021/acs.jctc.6c00228
J. Chem. Theory Comput. 2026, 22, 4802−4812

■ ACKNOWLEDGMENTS

This work was funded by the National Science Foundation under grant and CHE-2247583. We thank XSEDE for the necessary computational resources for all calculations involved in this project.

■ REFERENCES

(1) Gordon, S.; Hart, E. J.; Matheson, M. S.; Rabani, J.; Thomas, J. K. Reactions of the hydrated electron. *Discuss. Faraday Soc.* **1963**, *36*, 193−205.
(2) Marcus, R. A. Theory of Electron-Transfer Reaction Rates of Solvated Electrons. *J. Chem. Phys.* **1965**, *43*, 3477−3489.
(3) Siefermann, K. R.; Abel, B. The Hydrated Electron: A Seemingly Familiar Chemical and Biological Transient. *Angew. Chem., Int. Ed.* **2011**, *50*, 5264−5272.
(4) Ma, J.; Wang, F.; Denisov, S. A.; Adhikary, A.; Mostafavi, M. Reactivity of prehydrated electrons toward nucleobases and nucleotides in aqueous solution. *Sci. Adv.* **2017**, *3*, No. e1701669.
(5) Gu, J.; Leszczynski, J.; Schaefer, H. F. I. I. I. Interactions of Electrons with Bare and Hydrated Biomolecules: From Nucleic Acid Bases to DNA Segments. *Chem. Rev.* **2012**, *112*, 5603−5640.
(6) Herbert, J. M.; Coons, M. P. The Hydrated Electron. *Annu. Rev. Phys. Chem.* **2017**, *68*, 447−472.
(7) Janik, D.; Janik, I.; Bartels, D. M. Neutron and β/γ Radiolysis of Water up to Supercritical Conditions. 1. β/γ Yields for H2, H● Atom, and Hydrated Electron. *J. Phys. Chem. A* **2007**, *111*, 7777−7786.
(8) Le Caër, S. Water Radiolysis: Influence of Oxide Surfaces on H2 Production under Ionizing Radiation. *Water* **2011**, *3*, 235−253.
(9) McGrady, J.; Yamashita, S.; Kano, S.; Yang, H.; Kimura, A.; Taguchi, M.; Abe, H. Radiolysis of water at the surface of ZrO2 nanoparticles. *Radiat. Phys. Chem.* **2023**, *209*, 110970.
(10) Jordan, C. J. C.; Coons, M. P.; Herbert, J. M.; Verlet, J. R. R. Spectroscopy and dynamics of the hydrated electron at the water/air interface. *Nat. Commun.* **2024**, *15*, 182.
(11) Casey, J. R.; Schwartz, B. J.; Glover, W. J. Free Energies of Cavity and Noncavity Hydrated Electrons Near the Instantaneous Air/Water Interface. *J. Phys. Chem. Lett.* **2016**, *7*, 3192−3198.
(12) Sagar, D. M.; Bain, C. D.; Verlet, J. R. R. Hydrated Electrons at the Water/Air Interface. *J. Am. Chem. Soc.* **2010**, *132*, 6917−6919.
(13) Matsuzaki, K.; Kusaka, R.; Nihonyanagi, S.; Yamaguchi, S.; Nagata, T.; Tahara, T. Partially Hydrated Electrons at the Air/Water Interface Observed by UV-Excited Time-Resolved Heterodyne-Detected Vibrational Sum Frequency Generation Spectroscopy. *J. Am. Chem. Soc.* **2016**, *138*, 7551−7557.
(14) Hart, E. J. The Hydrated Electron. *Science* **1964**, *146*, 19−25.
(15) Neupane, P.; Bartels, D. M.; Thompson, W. H. Exploring the Unusual Reactivity of the Hydrated Electron with CO2. *J. Phys. Chem. B* **2024**, *128*, 567−575.
(16) Novelli, F.; Chen, K.; Buchmann, A.; Ockelmann, T.; Hoberg, C.; Head-Gordon, T.; Havenith, M. The birth and evolution of solvated electrons in the water. *Proc. Natl. Acad. Sci. U. S. A.* **2023**, *120*, No. e2216480120.
(17) Elkins, M. H.; Williams, H. L.; Shreve, A. T.; Neumark, D. M. Relaxation Mechanism of the Hydrated Electron. *Science* **2013**, *342*, 1496−1499.
(18) Bragg, A. E.; Verlet, J. R. R.; Kammrath, A.; Cheshnovsky, O.; Neumark, D. M. Hydrated Electron Dynamics: From Clusters to Bulk. *Science* **2004**, *306*, 669−671.
(19) Borrelli, W. R.; Mei, K. J.; Park, S. J.; Schwartz, B. J. Partial Molar Solvation Volume of the Hydrated Electron Simulated Via DFT. *J. Phys. Chem. B* **2024**, *128*, 2425−2431.
(20) Neupane, P.; Bartels, D. M.; Thompson, W. H. Relation between the Hydrated Electron Solvation Structure and Its Partial Molar Volume. *J. Phys. Chem. B* **2023**, *127*, 5941−5947.
(21) Park, S. J.; Narvaez, W. A.; Schwartz, B. J. How Water−Ion Interactions Control the Formation of Hydrated Electron:Sodium Cation Contact Pairs. *J. Phys. Chem. B* **2021**, *125*, 13027−13040.
(22) Copeland, D. A.; Kestner, N. R.; Jortner, J. Excess Electrons in Polar Solvents. *J. Chem. Phys.* **1970**, *53*, 1189−1216.
(23) Uhlig, F.; Marsalek, O.; Jungwirth, P. Unraveling the Complex Nature of the Hydrated Electron. *J. Phys. Chem. Lett.* **2012**, *3*, 3071−3075.
(24) Lan, J.; Rybkin, V. V.; Pasquarello, A. Temperature Dependent Properties of the Aqueous Electron. *Angew. Chem., Int. Ed.* **2022**, *61*, No. e202209398.
(25) Kratz, S.; Torres-Alacan, J.; Urbanek, J.; Lindner, J.; Vöhringer, P. Geminate recombination of hydrated electrons in liquid-to-supercritical water studied by ultrafast time-resolved spectroscopy. *Phys. Chem. Chem. Phys.* **2010**, *12*, 12169−12176.
(26) Bartels, D. M.; Takahashi, K.; Cline, J. A.; Marin, T. W.; Jonah, C. D. Pulse Radiolysis of Supercritical Water. 3. Spectrum and Thermodynamics of the Hydrated Electron. *J. Phys. Chem. A* **2005**, *109*, 1299−1307.
(27) Nicolas, C.; Boutin, A.; Lévy, B.; Borgis, D. Molecular simulation of a hydrated electron at different thermodynamic state points. *J. Chem. Phys.* **2003**, *118*, 9689−9696.
(28) Borsarelli, C. D.; Bertolotti, S. G.; Previtali, C. M. Thermodynamic changes associated with the formation of the hydrated electron after photoionization of inorganic anions: a time-resolved photoacoustic study. *Photochem. Photobiol. Sci.* **2003**, *2*, 791−795.
(29) Boero, M. Excess Electron in Water at Different Thermodynamic Conditions. *J. Phys. Chem. A* **2007**, *111*, 12248−12256.
(30) Larsen, R. E.; Schwartz, B. J. Full Configuration Interaction Computer Simulation Study of the Thermodynamic and Kinetic Stability of Hydrated Dielectrons. *J. Phys. Chem. B* **2006**, *110*, 1006−1014.
(31) Borrelli, W. R.; Liu, X.; Schwartz, B. J. The Solvation Entropy of Different Simulation Models of the Hydrated Electron. *J. Phys. Chem. Lett.* **2026**, *17*, 1899.
(32) Zho, C.-C.; Farr, E. P.; Glover, W. J.; Schwartz, B. J. Temperature dependence of the hydrated electron's excited-state relaxation. I. Simulation predictions of resonance Raman and pump-probe transient absorption spectra of cavity and non-cavity models. *J. Chem. Phys.* **2017**, *147*, 074503.
(33) Park, S. J.; Schwartz, B. J. Understanding the Temperature Dependence and Finite Size Effects in Ab Initio MD Simulations of the Hydrated Electron. *J. Chem. Theory Comput.* **2022**, *18*, 4973−4982.
(34) Narvaez, W. A.; Neupane, P.; Bartels, D. M.; Thompson, W. H. Ab Initio Molecular Dynamics Study of the Reduction of Acetone by the Hydrated Electron. *J. Phys. Chem. B* **2025**, *129*, 8201−8209.
(35) Samejo, B. A.; Rayaroth, M. P.; Wang, C.; Sun, X.; Boczkaj, G. Hydrated electrons and other reductive species - properties, formation and applications in advanced reduction processes for degradation of emerging organic pollutants − a review. *Water Resour. Ind.* **2025**, *34*, 100311.
(36) Biswas, S.; Wang, X.; Wong, B. M. Advanced experimental and computational approaches for advanced reduction of per- and polyfluoroalkyl substances. *Curr. Opin. Chem. Eng.* **2024**, *44*, 101017.
(37) Biswas, S.; Yamijala, S. S. R. K. C.; Wong, B. M. Degradation of Per- and Polyfluoroalkyl Substances with Hydrated Electrons: A New Mechanism from First-Principles Calculations. *Environ. Sci. Technol.* **2022**, *56*, 8167−8175.
(38) Garrett, B. C.; et al. Role of Water in Electron-Initiated Processes and Radical Chemistry: Issues and Scientific Advances. *Chem. Rev.* **2005**, *105*, 355−390.
(39) Bartels, D. M.; Craw, M. T.; Han, P.; Trifunac, A. D. Hydrogen/deuterium isotope effects in water radiolysis. 1. The mechanism of chemically induced dynamic electron polarization generation in spurs. *J. Phys. Chem.* **1989**, *93*, 2412−2421.
(40) Han, P.; Bartels, D. M. Hydrogen/deuterium isotope effects in water radiolysis. 2. Dissociation of electronically excited water. *J. Phys. Chem.* **1990**, *94*, 5824−5833.

https://doi.org/10.1021/acs.jctc.6c00228
J. Chem. Theory Comput. 2026, 22, 4802−4812

(41) Han, P.; Bartels, D. M. Hydrogen/deuterium isotope effects in water radiolysis. 3. Atomic hydrogen in acidic water/water-d2 mixtures. *J. Phys. Chem.* **1991**, *95*, 9370−9374.
(42) Han, P.; Bartels, D. M. Hydrogen/deuterium isotope effects in water radiolysis. 4. The mechanism of aquated hydrogen atom.-dblharw. solvated electron [(H)aq.dblharw. (e-)aq] interconversion. *J. Phys. Chem.* **1992**, *96*, 4899−4906.
(43) Buttersack, T.; et al. Photoelectron spectra of alkali metal−ammonia microjets: From blue electrolyte to bronze metal. *Science* **2020**, *368*, 1086−1091.
(44) Hartweg, S.; Barnes, J.; Yoder, B. L.; Garcia, G. A.; Nahon, L.; Miliordos, E.; Signorell, R. Solvated dielectrons from optical excitation: An effective source of low-energy electrons. *Science* **2023**, *380*, 1161−1165.
(45) Mei, K. J.; Borrelli, W. R.; Sandoval, J. L. G.; Schwartz, B. J. How to Probe Hydrated Dielectrons Experimentally: Ab Initio Simulations of the Absorption Spectra of Aqueous Dielectrons, Electron Pairs, and Hydride. *J. Phys. Chem. Lett.* **2024**, *15*, 9557−9565.
(46) Nemirovich, T.; Kostal, V.; Copko, J.; Schewe, H. C.; Boháčová, S.; Martinek, T.; Slanina, T.; Jungwirth, P. Bridging Electrochemistry and Photoelectron Spectroscopy in the Context of Birch Reduction: Detachment Energies and Redox Potentials of Electron, Dielectron, and Benzene Radical Anion in Liquid Ammonia. *J. Am. Chem. Soc.* **2022**, *144*, 22093−22100.
(47) Gao, L.; Zhang, L.; Fu, Q.; Bu, Y. Molecular Dynamics Characterization of Dielectron Hydration in Liquid Water with Unique Double Proton Transfers. *J. Chem. Theory Comput.* **2021**, *17*, 666−677.
(48) Borrelli, W. R.; Sandoval, J. L. G.; Mei, K. J.; Schwartz, B. J. Roles of H-Bonding and Hydride Solvation in the Reaction of Hydrated (Di)electrons with Water to Create H2 and OH. *J. Chem. Theory Comput.* **2024**, *20*, 7337.
(49) Schmidt, K. H.; Bartels, D. M. Lack of ionic strength effect in the recombination of hydrated electrons:(e)aq + (e)aq → 2(OH) + H2. *Chem. Phys.* **1995**, *190*, 145−152.
(50) Barnett, R. N.; Giniger, R.; Cheshnovsky, O.; Landman, U. Dielectron Attachment and Hydrogen Evolution Reaction in Water Clusters. *J. Phys. Chem. A* **2011**, *115*, 7378−7391.
(51) Marin, T. W.; Takahashi, K.; Jonah, C. D.; Chemerisov, S. D.; Bartels, D. M. Recombination of the Hydrated Electron at High Temperature and Pressure in Hydrogenated Alkaline Water. *J. Phys. Chem. A* **2007**, *111*, 11540−11551.
(52) Park, S. J.; Narvaez, W. A.; Schwartz, B. J. Ab Initio Studies of Hydrated Electron/Cation Contact Pairs: Hydrated Electrons Simulated with Density Functional Theory Are Too Kosmotropic. *J. Phys. Chem. Lett.* **2023**, *14*, 559−566.
(53) Kühne, T. D.; Iannuzzi, M.; Del Ben, M.; Rybkin, V. V.; Seewald, P.; Stein, F.; Laino, T.; Khaliullin, R. Z.; Schütt, O.; Schiffmann, F.; et al. CP2K: An electronic structure and molecular dynamics software package - Quickstep: Efficient and accurate electronic structure calculations. *J. Chem. Phys.* **2020**, *152*, 194103.
(54) Martyna, G. J.; Klein, M. L.; Tuckerman, M. Nosé−Hoover chains: The canonical ensemble via continuous dynamics. *J. Chem. Phys.* **1992**, *97*, 2635−2643.
(55) Park, S. J.; Schwartz, B. J. How Ions Break Local Symmetry: Simulations of Polarized Transient Hole Burning for Different Models of the Hydrated Electron in Contact Pairs with Na+. *J. Phys. Chem. Lett.* **2023**, *14*, 3014−3022.
(56) Pizzochero, M.; Ambrosio, F.; Pasquarello, A. Picture of the wet electron: a localized transient state in liquid water. *Chem. Sci.* **2019**, *10*, 7442−7448.
(57) Perdew, J. P.; Ernzerhof, M.; Burke, K. Rationale for mixing exact exchange with density functional approximations. *J. Chem. Phys.* **1996**, *105*, 9982−9985.
(58) Grimme, S.; Antony, J.; Ehrlich, S.; Krieg, H. A consistent and accurate ab initio parametrization of density functional dispersion correction (DFT-D) for the 94 elements H-Pu. *J. Chem. Phys.* **2010**, *132*, 154104.
(59) Guidon, M.; Hutter, J.; VandeVondele, J. Auxiliary Density Matrix Methods for HartreeFock Exchange Calculations. *J. Chem. Theory Comput.* **2010**, *6*, 2348−2364.
(60) Dai, C.; Li, K.; Liu, Y.; Teng, B.; Chen, Q.; Jin, X.; Xu, D.; Hong, R. Unveiling the directional dynamics: Hydrated electron driven defluorination in $PFOA^-$ and $PFOS^-$ through ab Initio molecular dynamics and quantum chemistry. *Water Res.* **2025**, *280*, 123486.
(61) Li, K.; Chen, Z.; Jin, X.; Tian, H.; Song, Z.; Zhang, Q.; Xu, D.; Hong, R. Theoretical investigation of Aryl/Alkyl halide reduction with hydrated electrons from energy and AIMD aspects. *J. Mol. Model.* **2023**, *29*, 142.
(62) Ambrosio, F.; Miceli, G.; Pasquarello, A. Electronic Levels of Excess Electrons in Liquid Water. *J. Phys. Chem. Lett.* **2017**, *8*, 2055−2059.
(63) Bernas, A.; Ferradini, C.; Jay-Gerin, J.-P. On the electronic structure of liquid water: Facts and reflections. *Chem. Phys.* **1997**, *222*, 151−160.
(64) Borrelli, W. R.; Liu, X.; Schwartz, B. J. How the choice of exchange−correlation functional affects DFT-based simulations of the hydrated electron. *J. Chem. Phys.* **2025**, *162*, 110901.
(65) Han, P.; Bartels, D. M. On the hydrated electron as a structure-breaking ion. *J. Phys. Chem.* **1991**, *95*, 5367−5370.
(66) Janik, I.; Lisovskaya, A.; Bartels, D. M. Partial Molar Volume of the Hydrated Electron. *J. Phys. Chem. Lett.* **2019**, *10*, 2220−2226.
(67) Borrelli, W. R.; Sandoval, J. L. G.; Schwartz, B. J. Using Density-Corrected DFT to Understand Density-Driven and Functional-Dependent Errors in Ab Initio Simulations of the Hydrated Electron. *J. Chem. Theory Comput.* **2026**, *22*, 2550−2561.
(68) Migus, A.; Gauduel, Y.; Martin, J. L.; Antonetti, A. Excess electrons in liquid water: First evidence of a prehydrated state with femtosecond lifetime. *Phys. Rev. Lett.* **1987**, *58*, 1559−1562.
(69) Kee, T. W.; Son, D. H.; Kambhampati, P.; Barbara, P. F. A Unified Electron Transfer Model for the Different Precursors and Excited States of the Hydrated Electron. *J. Phys. Chem. A* **2001**, *105*, 8434−8439.
(70) Savolainen, J.; Uhlig, F.; Ahmed, S.; Hamm, P.; Jungwirth, P. Direct observation of the collapse of the delocalized excess electron in water. *Nat. Chem.* **2014**, *6*, 697−701.
(71) Humphrey, W.; Dalke, A.; Schulten, K. VMD: Visual molecular dynamics. *J. Mol. Graphics* **1996**, *14*, 33−38.
(72) Turi, L.; Gaigeot, M.-P.; Levy, N.; Borgis, D. Analytical investigations of an electron−water molecule pseudopotential. I. Exact calculations on a model system. *J. Chem. Phys.* **2001**, *114*, 7805−7815.
(73) Turi, L.; Borgis, D. Analytical investigations of an electron−water molecule pseudopotential. II. Development of a new pair potential and molecular dynamics simulations. *J. Chem. Phys.* **2002**, *117*, 6186−6195.
(74) Berendsen, H. J. C.; Postma, J. P. M.; van Gunsteren, W. F.; Hermans, J. In Intermolecular Forces. *Proceedings of the Fourteenth Jerusalem Symposium on Quantum Chemistry and Biochemistry Held in Jerusalem, Israel, April 13−16, 1981*; Pullman, B., Ed.; Springer Netherlands, 1981; pp 331−342.
(75) Larsen, R. E.; Schwartz, B. J. Mixed Quantum/Classical Molecular Dynamics Simulations of the Hydrated Dielectron: The Role of Exchange in Condensed-Phase Structure, Dynamics, and Spectroscopy. *J. Phys. Chem. B* **2004**, *108*, 11760−11773.
(76) Virtanen, P.; et al. SciPy 1.0: Fundamental Algorithms for Scientific Computing in Python. *Nat. Methods* **2020**, *17*, 261−272.
(77) Rybkin, V. V. Mechanism of Aqueous Carbon Dioxide Reduction by the Solvated Electron. *J. Phys. Chem. B* **2020**, *124*, 10435−10441.
(78) Lan, J.; Kapil, V.; Gasparotto, P.; Ceriotti, M.; Iannuzzi, M.; Rybkin, V. V. Simulating the ghost: quantum dynamics of the solvated electron. *Nat. Commun.* **2021**, *12*, 766.
(79) Narvaez, W. A.; Park, S. J.; Schwartz, B. J. Hydrated Electrons in High-Concentration Electrolytes Interact with Multiple Cations: A Simulation Study. *J. Phys. Chem. B* **2022**, *126*, 3748−3757.

https://doi.org/10.1021/acs.jctc.6c00228
J. Chem. Theory Comput. 2026, 22, 4802−4812

(80) Borgis, D.; Rossky, P. J.; Turi, L. Nuclear quantum effects on the nonadiabatic decay mechanism of an excited hydrated electron. *J. Chem. Phys.* **2007**, *127*, 174508.
(81) Tay, K. A.; Boutin, A. Hydrated Electron Diffusion: The Importance of Hydrogen-Bond Dynamics. *J. Phys. Chem. B* **2009**, *113*, 11943−11949.
(82) Turi, L.; Ádám, M.; Rossky, P. J. Excess electron localization sites in neutral water clusters. *J. Chem. Phys.* **2006**, *125*, 014308.
(83) Turi, L.; Sheu, W.-S.; Rossky, P. J. Characterization of Excess Electrons in Water-Cluster Anions by Quantum Simulations. *Science* **2005**, *309*, 914−917.

https://doi.org/10.1021/acs.jctc.6c00228
J. Chem. Theory Comput. 2026, 22, 4802−4812